Downloaded from jnm.snmjournals.org by on March 14, 2017. For personal use only.

Multimodal Assessment of In Vivo Metabolism with Hyperpolarized [1-^{13}C]MR Spectroscopy and ^{18}F-FDG PET Imaging in Hepatocellular Carcinoma Tumor–Bearing Rats

Marion I. Menzel*[1], Eliane V. Farrell*[2], Martin A. Janich[1], Oleksandr Khegai[1,3], Florian Wiesinger[1], Stephan Nekolla[2], Angela M. Otto[4], Axel Haase[4], Rolf F. Schulte[1], and Markus Schwaiger[2]

[1]GE Global Research, Munich, Germany; [2]Department of Nuclear Medicine, Technische Universität München, Munich, Germany; [3]Department of Chemistry, Technische Universität München, Munich, Germany; and [4]Department of Medical Engineering, Technische Universität München, Munich, Germany

Abnormalities of tumor metabolism can be exploited for molecular imaging. PET imaging of ^{18}F-FDG is a well-established method using the avid glucose uptake of tumor cells. ^{13}C MR spectroscopic imaging (MRSI) of hyperpolarized [1-^{13}C]pyruvate and its metabolites, meanwhile, represents a new method to study energy metabolism by visualizing, for example, the augmented lactate dehydrogenase activity in tumor cells. Because of rapid signal loss, this method underlies strict temporal limitations, and the acquisition of data—encoding spatial, temporal, and spectral information within this time frame—is challenging. The object of our study was to compare spectroscopic images with ^{18}F-FDG PET images for visualizing tumor metabolism in a rat model. **Methods:** ^{13}C MRSI with IDEAL (Iterative Decomposition of water and fat with Echo Asymmetry and Least-squares estimation) chemical shift imaging in combination with single-shot spiral acquisition was used to obtain dynamic data from 23 rats bearing a subcutaneous hepatocellular carcinoma and from reference regions of the same animals. Static and dynamic analysis of ^{18}F-FDG PET images of the same animals was performed. The data were analyzed qualitatively (visual assessment) and quantitatively (magnitude and dynamics of ^{18}F-FDG uptake, ^{13}C MRSI dynamics, and physiologic parameters). **Results:** In most animals increased [1-^{13}C]lactate signals in the tumor could be detected by simple display of integrated [1-^{13}C]lactate images with corresponding enhanced ^{18}F-FDG uptake. Low [1-^{13}C]pyruvate or [1-^{13}C]lactate signals did not correlate with histologic or physiologic parameters. Significantly less pyruvate reached the tumors than the gastrointestinal tract, but in tumors a significantly higher amount of pyruvate was converted to lactate and alanine within seconds after intravenous administration. **Conclusion:** This study reveals that PET and ^{13}C MRSI can be used to visualize increased glycolytic flux in malignant tissue. The combination of signals will allow the quantitative dissection of substrate metabolism, with respect to uptake and downstream metabolic pathways. Although hyperpolarized [1-^{13}C]pyruvate increases the sensitivity of MR imaging, signal-to-noise ratio constraints still apply for spatially and temporally resolved ^{13}C MRSI, emphasizing the need for further MR methodologic development. These first imaging data suggest the feasibility of ^{13}C MRSI for future clinical use.

Received Aug. 14, 2012; revision accepted Jan. 14, 2013.
For correspondence or reprints contact: Eliane V. Farrell, Technische Universität München, Department of Nuclear Medicine, Ismaninger Strasse 22, D-81675 Munich, Germany.
E-mail: eliane.farrell@tum.de
*Contributed equally to this work.
Published online Apr. 17, 2013.
COPYRIGHT © 2013 by the Society of Nuclear Medicine and Molecular Imaging, Inc.

Key Words: animal imaging; molecular imaging; MR imaging; PET; ^{13}C

J Nucl Med 2013; 54:1113–1119
DOI: 10.2967/jnumed.112.110825

Cancer metabolism differs from that of the surrounding tissue, constituting the basis for tumor-specific biochemical imaging strategies for the past 40 y. Tumor cells have an increased energy demand, compared with other tissue, to fuel proliferation. They also rely more on conversion of glucose to lactate than on oxidation of glucose, and this phenomenon, known as the Warburg effect, occurs even in the presence of sufficient oxygen (*1*).

The first principle is used in ^{18}F-FDG PET imaging: FDG radiolabeled with ^{18}F follows the same metabolic pathway as glucose (*2*). It is transported into the cell by glucose transporters (GLUTs) (*3*), where it is phosphorylated by hexokinase to ^{18}F-FDG-6-phosphate. Unlike glucose, the compound cannot be further metabolized, and ^{18}F-FDG-6-phosphate is trapped into the cell (*4*).

To date, ^{18}F-FDG is the most commonly used PET tracer and has been established as a gold standard for staging, restaging, monitoring treatment response, and detecting recurrence for a wide variety of cancers (*5,6*). One drawback of this method is ^{18}F-FDG uptake by inflammatory processes, which can confound the diagnosis of malignant lesions (*7*) and mask the initial success of antitumor therapies when tumors respond to therapy with inflammation (*8*).

^{13}C metabolic MR spectroscopic imaging (MRSI) of hyperpolarized substances is a novel imaging method to assess tumor metabolism in vivo that relinquishes radiation (*9–11*). With ^{13}C MR spectroscopy, signals from molecules within a tissue can be distinguished on the basis of their chemical shift. The application of conventional ^{13}C MR spectroscopy in vivo, however, has been hampered by its low sensitivity, leading to low signal-to-noise ratios (SNRs) in vivo. This low SNR in turn requires the acquisition of data from relatively large voxels, leading to low spatial resolution, or the acquisition of multiple averages, leading to low temporal resolution (*12*). The introduction of dynamic nuclear polarization increased sensitivity 10,000-fold, and in vivo imaging of the distribution of a hyperpolarized substance and its metabolic conversion has now become feasible (*13,14*).

Downloaded from jnm.snmjournals.org by on March 14, 2017. For personal use only.

The most commonly used agent for hyperpolarization is [1-^{13}C] pyruvate; it plays an important role in cellular energy metabolism, has a sufficiently long T_1 (30–40 s) relaxation time, and has a fast metabolism. Mediated by alanine transaminase and lactate dehydrogenase (LDH), the ^{13}C label of [1-^{13}C]pyruvate is exchanged with the preexisting alanine and lactate pool, or it can be converted irreversibly to [1-^{13}C]-carbon dioxide via pyruvate dehydrogenase, which is in equilibrium with [1-^{13}C]-bicarbonate (*15*). In line with the Warburg effect, pyruvate decarboxylation is decreased in tumor cells through upregulation of pyruvate dehydrogenase kinase, and pyruvate reduction is increased several-fold, compared with normal tissue, through the overexpression of LDH-A (*16*). MR spectroscopy of hyperpolarized [1-^{13}C]pyruvate can detect the resulting increase in lactate labeling, discerning tumor tissue (*11,13*). Intratumoral lactate levels correlate with the grade of malignancy (*17*) and metastatic potential and correlate inversely with patient survival (*18*).

On the basis of these observations, the noninvasive identification of increased lactate production in tumor tissue may be a valuable clinical signal for the management of patients with cancer (*19*).

Most experimental [1-^{13}C]pyruvate data are acquired with dedicated coils located over tumor tissue to dynamically acquire local spectra, which are used for metabolic analysis. The relatively fast and irreversible decay of the hyperpolarized MR signal imposes a great challenge for acquisition methods used for spectroscopic imaging, which requires encoding in 5 dimensions (3 spatial, 1 temporal, and 1 spectral) to be accomplished within less than 1 min (*20–23*).

To evaluate the diagnostic relevance of hyperpolarized ^{13}C MRSI in an animal model of hepatocellular carcinoma (HCC), we compared first results from dynamic ^{18}F-FDG PET imaging with those of hyperpolarized metabolic spectroscopic imaging using [1-^{13}C]pyruvate. ^{13}C MRSI of pyruvate metabolism aims to visualize multiple metabolic pathways dynamically. Pyruvate conversion to different metabolites (alanine, lactate, CO_2) and uptake into the cell are reversible, depending on metabolic state, perfusion, and product concentration. Necessitated by SNR limitations, a supraphysiologic amount of substance is injected, on the verge of saturating the biologic system in various organs (*24*). Imaging has to be accomplished shortly (i.e., within seconds) after injection of the short-lived hyperpolarized substance at a time at which most of the hyperpolarized pyruvate is still circulating in the blood pool (*25*).

In this study, we compared lactate-to-pyruvate ratios (LPRs) as markers of glycolytic lactate production with regional ^{18}F-FDG uptake; because of the high variability between signal intensities (caused by varying receiver gain, shimming, and polarization levels), it is difficult to assess absolute signal intensities. Therefore, it is beneficial to calculate ratios in which these differences are cancelled out. In addition, region-of-interest (ROI)–voxelwise analysis of ^{13}C uptake and conversion dynamics for selected ROIs in the tumor, vena cava, and gastrointestinal tract (GIT) was performed.

MATERIALS AND METHODS

Tumor Model and Animal Protocol

In twenty-six 6-wk-old male Buffalo rats (Harlan Winkelmann), subcutaneous tumors were induced by injection of the 1×10^6 syngeneic HCC cell line McA-RH7777 into the left flank. Tumors were allowed to grow for 10–19 d (mean, 14 d) and imaged with a diameter of approximately 1 cm (mean volume, 695 ± 167 mm^3). Of 26 animals, 1 was excluded because the tumor size was too small for imaging (<100 mm^3 tumor volume). Two animals were excluded because of respiratory problems associated with the tracer injection and a delayed time to peak (TTP) of tumor ^{13}C MRSI data. In these 2 animals, only [1-^{13}C]pyruvate could be detected in relevant amounts after [1-^{13}C]pyruvate injection, and the [1-^{13}C]pyruvate signal was localized almost entirely in the vena cava. We postulated embolization of a blood clot after intravenous injection as a possible explanation for the observations.

All animals underwent ^{18}F-FDG PET and ^{13}C MR metabolic imaging on consecutive days (23 ± 4 h). In 8 rats, ^{18}F-FDG PET was performed before MR measurements and in 15 after MR measurements.

Anesthesia was performed with 2% isoflurane during imaging. Blood samples were taken from the tail vein before ^{18}F-FDG injection and analyzed for glucose content (Accutrend Plus; Roche). Blood samples taken before and after [1-^{13}C]pyruvate injection were analyzed for glucose and lactate content. All procedures involving animals were approved by the animal care committee of the government of Bavaria, Germany.

Time of anesthesia before PET imaging started was short (21 ± 2 min), but data were acquired over a period of 60 min. Time of anesthesia before MRSI was longer (77 ± 3 min); however, imaging was accomplished within 2 min.

^{18}F-FDG PET Data Acquisition and Image Reconstruction

Rats were imaged with the Inveon small-animal PET/CT scanner (Siemens), starting with the intravenous injection of ^{18}F-FDG (6.09–22.45 MBq). Three-dimensional PET data were acquired for 60 min in list-mode, followed by low-dose CT acquisition of 120 projections obtained with an exposure time of 200 ms, x-ray voltage of 80 kVp, and anode current of 500 μA for a 220° rotation.

For tracer delivery analysis, PET data were sorted into 21 serial image frames consisting of 12 × 10, 1 × 20, 3 × 30, 1 × 135, 3 × 240, and 1 × 2,520 s. For the Patlak plot, data were summed into 9 frames consisting of 3 × 10, 1 × 570, and 5 × 600 s each. PET data were reconstructed using an ordered-subset expectation 3-dimensional algorithm with 2 iterations and 16 subsets. Counts were converted to Bq/cm^3 using a calibration factor derived from measurements of a rat-size phantom. The resulting matrices were 128 × 128 pixels with 159 transverse slices in a transaxial field of view (FOV) of 12.7 cm (pixel size, 0.77 × 0.77 × 0.80 mm). Data were normalized and corrected for randoms, dead time, and decay. No corrections were made for attenuation or scatter, as previously described (*26*). CT images were reconstructed using a modified Feldkamp algorithm. The resulting matrix was 256 × 256 pixels with 384 transverse slices (pixel size, 0.17 × 0.17 × 0.17 mm). For visual inspection, PET images were summed using data from 50 to 60 min of measurement.

Hyperpolarization

[1-^{13}C]pyruvic acid (14 M; Cambridge Isotope Laboratories), OX063 trityl radical (15 mM; Oxford Instruments), and Dotarem (10 mM; Guerbet) were mixed and polarized for 60–120 min, using a HyperSense dynamic nuclear polarizer (Oxford Instruments) according to the study of Adenkjaer-Larsen et al. (*13*). The polarized sample was dissolved with NaOH (80 mM), Tris buffer (80 mM; Sigma Aldrich), and Na_2-ethylenediaminetetraacetic acid (0.1 g/L; Sigma Aldrich), yielding 80 mM hyperpolarized [1-^{13}C]pyruvate solution (pH ≈7.5). Polarization levels were 19%–31% (mean ± SD, 24% ± 1%) using a Minispec mq40 nuclear magnetic resonance analyzer (Bruker Optik). Of the solution, 2.5 mL/kg (0.54 ± 0.01 mL per animal) were injected at a rate of 0.17 mL/s into the tail vein of the tumor-bearing animals, approximately 15 s after dissolution.

Downloaded from jnm.snmjournals.org by on March 14, 2017. For personal use only.

^{13}C MR Data Acquisition and Image Reconstruction

During MR measurements, rats were positioned on a heating pad, and the electrocardiogram heart rate, breathing rate, and rectal temperature were monitored (SA Instruments). A syringe filled with [1-^{13}C]lactate at thermal equilibrium polarization, as external signal reference, was also placed in the FOV. Experiments were performed on a Signa HDx 3 T MR imaging system (GE Healthcare) using a (diameter, 78 mm) dual-tuned ^{1}H/^{13}C radiofrequency coil (*27*) and whole-body gradient coil with a 23 mT/m maximum gradient amplitude and 77 T/m/s slew rate. Tumors were localized using standard ^{1}H imaging with 2-dimensional gradient echo acquisition in the axial, sagittal, and coronal orientations. Chemical shift imaging (CSI) was performed using a slice-selective IDEAL (Iterative Decomposition of water and fat with Echo Asymmetry and Least-squares estimation) spiral CSI sequence according to the study of Wiesinger et al. (*21*) for the encoding of spectral, spatial, and temporal information, with data acquired from a single transversal slice through the middle of the tumor. Imaging parameters were a FOV of 80 mm, flip angle of 10°, repetition time of 0.25 s, and slice thickness of 10 mm, using a 65-ms-long single-shot spiral readout for image encoding. Seven consecutive echo-shifted excitations (Δecho time, 1.12 ms) were used to encode chemical shift, preceded by a slice-selective free induction delay, resulting in an approximately 2-s duration for a single time step. This acquisition scheme was repeated 64 times, thus encoding 64 time points of the metabolic conversion, spanning approximately 2 min. Acquisition was started simultaneously with intravenous injection, so that the pyruvate uptake in the central vena cava could be monitored.

The primary data reconstruction was performed according to a previously published method (*21*), using MATLAB (MathWorks), resulting in reconstructed images of all metabolites (nominal resolution, 32×32, equivalent to a 5×5 mm^2 pixel size). [1-^{13}C]pyruvate, [1-^{13}C]lactate, and [1-^{13}C]alanine metabolite signals were integrated over time. As a reference for integration over 30 s, the maximum pyruvate signal in the vena cava was used. Integration started immediately after detection of the bolus, which typically occurred in the vena cava after 7–9 s. ^{13}C MR metabolite images were fused with corresponding proton MR images for subsequent display.

Image Analysis

The PET, MR, and ^{13}C MR spectroscopy images were fused and analyzed using the M3P Anima (Munich Heart) software. MR and PET images were coregistered visually, based on anatomic landmarks showing physiologic accumulation of ^{18}F-FDG, such as the kidneys, skin, tumor, and bone marrow. A registration matrix was saved and applied to the PET and ^{13}C spectroscopy images.

PET and ^{13}C MR images were visually examined, using the M3P Anima software package. Each PET and ^{13}C metabolite image was analyzed by placing ROIs over the tumor and the surrounding tissue, based on proton MR images

ROIs were drawn over the entire tumor area, including the necrotic part, and the dorsal muscle according to the anatomic proton MR images, covering the same transversal slices in the MR spectroscopy and PET images. The ROI was applied to the corresponding PET and spectroscopy images of the same animal. ^{18}F-FDG uptake was expressed as a tumor-to-muscle ratio (TMR) and mean standardized uptake value (SUVmean). Values obtained from the ^{13}C MR metabolite images were expressed in arbitrary units. TMRs and tumor LPRs were calculated for comparison with PET data.

^{18}F-FDG Patlak Graphical Analysis

Besides the calculation of SUVmean, ^{18}F-FDG uptake constant (K_i) was estimated by Patlak graphical analysis as described before (*28*), with data analyzed using Inveon Research Workplace (Siemens Medical Solutions). In brief, tumor ROIs and blood-activity ROIs over the left atrium were drawn and time–activity curves from these ROIs used for calculation of K_i and the metabolic rate of glucose assuming a lumped constant of 0.6.

Analysis of ^{13}C MR Metabolite Dynamics

Voxelwise analysis of [1-^{13}C]pyruvate, [1-^{13}C]lactate, and [1-^{13}C]alanine over the entire time course was conducted in voxels located centrally in ROIs that were placed manually on the vena cava, tumor, and GIT (Fig. 1). Maximum peak (MP) values were determined for pyruvate in the vena cava and for all metabolites in the tumor and GIT. The TTP (i.e., the relative delay between the MP of pyruvate in the vena cava and the MP of pyruvate in the target regions) was calculated. Similarly, the mean TTP between the MP of pyruvate and the MP of alanine and lactate for tumor and GIT was calculated, indicating time of conversion from pyruvate to its metabolites.

LDH Assay

The LDH levels in tumors of a subgroup of 5 animals were measured in vitro in tissue homogenate by photometric quantification of nicotinamide adenine dinucleotide oxidation, as described elsewhere (*29*). Tissue was homogenated and buffered, and the decrease in nicotinamide adenine dinucleotide absorbance was recorded at 340 nm at 22°C. The specific activity of LDH was expressed in units per milligram of protein. Nuclear density was measured with a CASY cell counter (CASYTT; Roche) (*29*).

Histology

Two slices through the center of the tumor were stained with hematoxylin and esosin. Immunohistochemical staining was analyzed with an image analysis platform (Enterprise Image Intelligence Suite; Definiens AG). Images were imported into the image analysis software, and necrosis was quantified. Necrotic areas and vital and connective tissue areas were calculated as the percentage of absolute tissue area.

Statistical Analysis

Correlations were checked with a Spearman's rank correlation coefficient. All results are displayed as the mean ± SEM.

RESULTS

The datasets of 23 animals weighing 215 ± 4 g were evaluated. Tumors at the time of imaging had a mean size of 695 ± 167 mm^3,

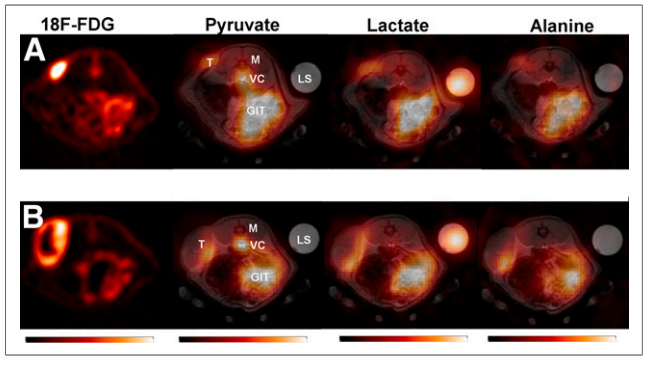

FIGURE 1. Examples of ^{13}C MR metabolite images (integrating 30 s) and PET images (summing 10 min). Color scale was windowed to 6 times background for [1-^{13}C]lactate images and to 10 times background for [1-^{13}C]pyruvate and [1-^{13}C]alanine images. (A) Tumor with high lactate TMR. (B) Tumor with high lactate TMR despite large necrotic part. K = kidney; LS = lactate syringe; M = muscle; T = tumor; VC = vena cava.

Downloaded from jnm.snmjournals.org by on March 14, 2017. For personal use only.

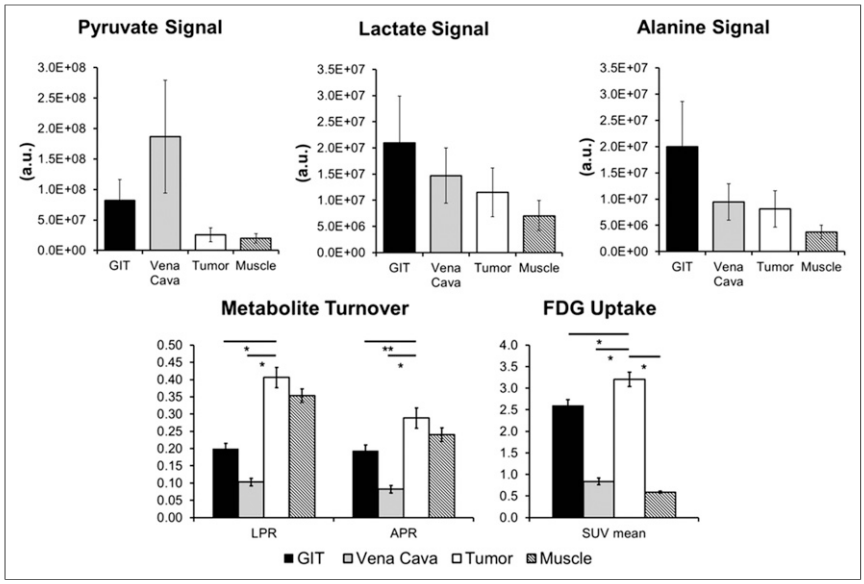

FIGURE 2. In vivo biodistribution of ^{13}C metabolites and ^{18}F-FDG in organs within FOV. APR = alanine-to-pyruvate ratio; a.u. = arbitrary units; SUV = standardized uptake value. *$P < 0.00001$. **$P = 0.015$.

ranging from 120 to 2,200 mm^3. Histology showed that slices through the center of the tumor covered a mean area of 68.2 ± 12.4 mm^2. This area was classified as follows: 13.3% ± 2.3% necrotic tissue, 64.2% ± 4.3% vital tissue, and 5.6% ± 1.9% connective tissue.

Quantification of ^{18}F-FDG Uptake and Analysis of ^{13}C Metabolite Dynamics

All 23 PET datasets showed pronounced ^{18}F-FDG uptake in tumors, which was easily distinguishable from the surrounding tissue (Fig. 1). The average TMR was 5.6 ± 0.3, and in tumors the average SUVmean was 3.2 ± 0.2, ranging from 1.9 to 4.5. SUVmean in the GIT, vena cava, and muscle was significantly lower (Fig. 2). The mean rate constant of ^{18}F-FDG transport (K_i) into tumor cells was 0.03 ± 0.002, with values ranging from 0.013 to 0.042, and the mean metabolic rate of glucose was 0.5 ± 0.03 μmol/g/min, varying from 0.19 to 0.65 μmol/g/min.

When ^{13}C MRSI dynamic data were analyzed, a rapidly occurring peak of [1-^{13}C]pyruvate signal was observed in the inferior vena cava after injection. [1-^{13}C]pyruvate TTP in the tumor was 9 ± 0.5 s after the blood peak, significantly later than in the GIT (7 ± 0.3 s, $P = 0.006$). Alanine and lactate peaked, with a time delay in tumor and GIT (alanine TTP in tumor and GIT was 25 ± 2 and 20 ± 1 s, respectively, and lactate TTP in tumor and GIT was 22 ± 1 and 21 ± 1 s, respectively). Conversion to alanine took place in the tumor significantly more slowly than in the GIT after the blood peak ($P = 0.02$) (Figs. 3 and 4).

In relation to the peak signal detected in the vena cava, the MP of pyruvate in the tumor was significantly lower than that in the GIT (relative MP of pyruvate in tumor to MP of pyruvate in the vena cava, 6% ± 1%, vs. relative MP of pyruvate in GIT to MP of pyruvate in the vena cava, 16% ± 3%; $P = 0.001$). But in relation to the MP of pyruvate detected in each organ, a significantly higher conversion to alanine and lactate took place in the tumor (relative MP of alanine in tumor to MP of pyruvate in tumor, 26% ± 3%, vs. relative MP of alanine in GIT to MP of pyruvate in GIT, 17% ± 1% [$P = 0.03$], and relative MP of lactate in tumor to MP of pyruvate in tumor, 36% ± 3%, vs. relative MP of lactate in GIT to MP of pyruvate in GIT, 20% ± 1% [$P = 0.0003$]) (Fig. 4).

For ^{13}C MRSI, the average TMR of [1-^{13}C]lactate was 1.8 ± 0.3, and the LPR of tumors was 0.4 ± 0.03. TMR showed a wide variety of values, ranging from 0.4 to 5.8, whereas the variety of LPR was comparable to SUVmean, ranging from 0.2 to 0.6. The analysis of ROIs over the organs in the FOV supported the results from dynamic data, insofar as total lactate signal in tumor ROIs was not significantly higher than that in muscle ROIs and even lower than in ROIs over the GIT and vena cava. However, metabolite turnover, as evaluated by the LPR, was significantly higher in tumor ROIs than in ROIs over the GIT and vena cava (Fig. 2). The cross-modality correlation coefficients for all datasets between TMR of ^{18}F-FDG and TMR of [1-^{13}C]lactate and between standardized uptake value (^{18}F-FDG) and the LPR (^{13}C MRSI) in the tumor were 0.13 and −0.22, respectively; no significant correlations were found.

LDH Activity

Lysed tumor tissue had a mean specific LDH activity of 0.11 ± 0.01 units of protein per milligram, a cellular density of 0.23 ± 0.01 million cells per milligram of tissue, and a cellular activity of 0.5 ± 0.04 units per million cells.

DISCUSSION

In this study, ^{13}C MRSI was performed using a novel IDEAL spiral CSI acquisition approach, which allows for time-resolved CSI (*21*) with a time resolution of 2 s.

The visual assessment of ^{13}C metabolite images derived from dynamic [1-^{13}C]pyruvate and [1-^{13}C]lactate spectra provided good imaging contrast in agreement with increased ^{18}F-FDG uptake in tumor tissue in most of the animals (Fig. 1). Intratumoral heterogeneities due to necrosis could be identified in the ^{13}C metabolic and ^{18}F-FDG images.

Low TMRs in [1-^{13}C]pyruvate and [1-^{13}C]lactate signals observed in some tumors did not correlate with physiologic differences in the animals (Table 1), and we observed that the tumor stage regarding size and grade of necrosis did not influence the ^{13}C signal to the same extent as Larson et al. reported previously (*30*). Tissue analysis for units of lysed LDH of a subgroup of the tumors showed no correlation to [1-^{13}C]lactate signal strength. However, the true LDH activity in intact tumor cells in vivo is likely to depend on more factors than just the concentration. The observed variance of CSI signals may be a consequence of methodologic and biologic issues. Besides delayed pyruvate delivery, decreased overall uptake of pyruvate in the tumors may have been present in these animals, despite similar delivery through the vena cava: as a result, tissue pyruvate and lactate concentrations in tumors were likely to be lower than the current detection levels of the used ^{13}C CSI technique using IDEAL (Fig. 4).

Downloaded from jnm.snmjournals.org by on March 14, 2017. For personal use only.

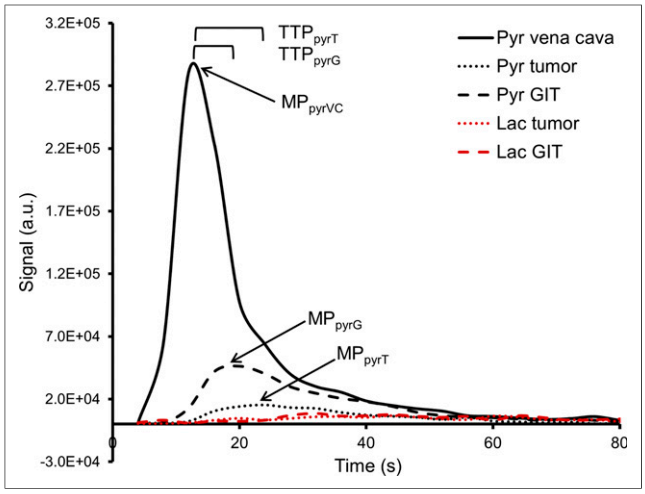

FIGURE 3. Exemplary dataset depicting signal of pyruvate bolus arriving in vena cava (MPpyrVC), tumor (MPpyrT), and GIT (MPpyrG). Arrival in tumor and GIT is delayed by [1-^{13}C]pyruvate TTP or TTPpyG, respectively. For simplicity, only pyruvate MP and TTP are annotated in figure; determination of lactate and alanine MP and TTP was performed accordingly. Lac = lactate; Pyr = pyruvate; TTPpyrT = time to peak of pyruvate in tumor: time difference between MP of pyruvate in vena cava and MP of pyruvate in tumor.

Furthermore, it is not possible to determine whether the detected ^{13}C metabolite signals originate from blood or extracellular or intracellular space. In ^{18}F-FDG PET measurements, origination of signal can be ascertained by choosing a late time point of measurement that guarantees tracer clearance from all but intracellular locations. In ^{13}C metabolic MR imaging, however, intra- and extracellular compartments contribute to the observed signal to varying but unknown proportions.

In theory, the observed [1-^{13}C]lactate signal should indicate that [1-^{13}C]pyruvate has been taken up into cells and has been intracellularly converted to [1-^{13}C]lactate by LDH. In tumor tissue, however, extracellular [1-^{13}C]pyruvate could be converted in necrotic areas. LDH is not inactivated when cells perish, and conversion of [1-^{13}C]pyruvate can therefore still take place in tumor regions without viable cells.

The analysis of ^{13}C metabolite dynamics, referencing [1-^{13}C]pyruvate peak signal intensities in the tumors to the vena cava and the GIT, revealed that a significantly smaller amount of [1-^{13}C]pyruvate reached the tumors than the GIT, most likely reflecting the lower perfusion of transplanted tumor cells in comparison to the reference organs. In contrast to delivery, however, more of the [1-^{13}C] label in tumor tissue was turned over to [1-^{13}C]lactate and [1-^{13}C]alanine than in the GIT, confirming the high metabolic activity of tumor tissue according to the Warburg effect (Fig. 4).

Darpolor et al. had already described a higher turnover of [1-^{13}C]pyruvate to [1-^{13}C]lactate and [1-^{13}C]alanine than with reference tissue; however, this turnover was in orthotopic tumors of the same cell line. They reported equal amounts of [1-^{13}C]pyruvate being delivered to healthy liver and to tumor tissue as opposed to the reduced delivery of pyruvate to the ectopic tumor model we observed. The manifold higher turnover to [1-^{13}C]lactate and [1-^{13}C]alanine in tumor, therefore, resulted in clearly distinguishable peaks (*31*). The liver is a highly perfused organ, and HCC tumors that are growing in the orthotopic location are well vascularized (*32*). Growth of these tumors in an ectopic location, with a different microenvironment and at a higher growth rate (700 mm^3 in 12–14 d, compared with 100–200 mm^3 as reported by Darpolor et al.), is likely to lead to a different grade of vascularization (*31,33*). Restricted vascularization in our model could explain the low amount of [1-^{13}C]pyruvate detected in the tumor region, compared with other organs in the FOV (GIT) and in the vena cava.

The tumor was detectable in most animals using integrated ^{13}C metabolite images. But because only a small fraction (2%) of the MP of pyruvate in the vena cava reached the tumors and was converted to lactate, in some cases effects such as slow bolus injection and reduced delivery and uptake of pyruvate in tumor tissue presumably result in significantly reduced contrast between tumor and background by simple visual assessment, as the observable spatially resolved signals in dynamic ^{13}C MRSI are at the verge of SNR. Furthermore, the ^{13}C MRSI protocol with respect to both acquisition parameters and injected dose of pyruvate (*24*) was optimized in healthy animals and for highly perfused organs such as the liver and kidneys, which turned out to be suboptimal for slower perfused tumors, because it is skewed toward the detection of vena cava pyruvate bolus instead of sparing magnetization for later time points. To overcome this SNR constraint in future studies, promising approaches exist: Schulte et al. recently introduced a saturation recovery MRSI sequence to provide parametric images for the quantitation of metabolic fluxes such as the conversion of pyruvate to lactate (*22*); alternatively spectral–spatial excitation approaches could be tailored for better SNR of [1-^{13}C]lactate (*34,35*).

Nonetheless, the calculation of turnover ratios of lactate to pyruvate within the tumor represents the unique feature of ^{13}C MRSI, as compared with ^{18}F-FDG PET radiotracer imaging. Tumor tissue showed a significantly higher conversion of pyruvate to lactate than the GIT (Figs. 2 and 4), highlighting the nonoxidative metabolism in malignant tissue. Furthermore, with the improved time resolution of the IDEAL spiral CSI acquisition, we could demonstrate the high tumor specificity of ^{13}C metabolite dynamics, which is supported by similar observations of Larson et al. (*30*).

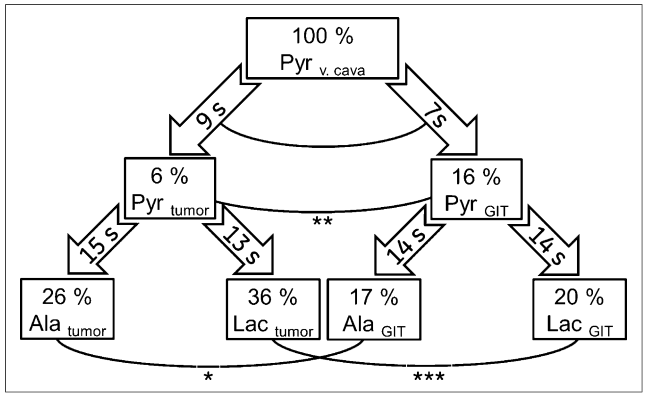

FIGURE 4. Analysis of ^{13}C metabolite dynamics in vena cava (v. cava), tumor, and GIT. Number of * depicts level of significance for MP and TTP for pairwise comparison of regions and metabolites, respectively. For conversion of pyruvate (Pyr) to lactate (Lac) and alanine (Ala) in target regions, relative TTP to arrival of pyruvate in respective region is depicted. *P = 0.03. **P = 0.005. ***P = 0.0002.

Downloaded from jnm.snmjournals.org by on March 14, 2017. For personal use only.

TABLE 1
Physiologic and Measurement Parameters and Their Correlation Coefficient with Parameters Quantifying Lactate Signal

Parameter	Mean ± SEM	Spearman's rank correlation coefficient	
		TMR of lactate	Tumor LPR
Blood lactate (mmol/L)			
Before pyruvate	2.4 ± 0.2	0.13	0.15
After pyruvate	2.7 ± 0.2	0.04	0.04
Blood glucose (mmol/L)			
Before pyruvate	173 ± 3.1	0.06	0.12
After pyruvate	192 ± 7.3	−0.02	0.04
Heart rate (bpm)	355 ± 5.5	−0.15	0.13
Breathing rate (per min)	59 ± 1.4	−0.05	0.08
Body temperature (°C)	37.4 ± 0.1	−0.37	0.23
Tumor size (mm^3)	616 ± 127.4	−0.04	−0.03
Duration of tumor growth (d)	14 ± 1	0.03	−0.44
Duration of anesthesia	1 h 17 ± 0:03 min	−0.26	0.25
Injected volume (mL/kg)	2.5 ± 0.03	0.27	−0.15
Time polarizer to injection (s)	15.1 ± 1.4	−0.05	0.08
Duration of injection (s)	3.2 ±0.1	0.52	0.19
Polarization level (%)	24.1± 0.1	−0.11	0.07

No significant correlations between parameters were observed.

For quantitative analysis, emphasis was placed on comparability of data from both modalities. Therefore, we copied the same ROI, covering the entire tumor to all metabolic images, and compared mean values derived from these images so that spatial heterogeneity and partial volume would have the same effects on the results. However, no significant correlation between PET and MRSI data was observed, for several possible reasons. The MR and PET studies were performed at different time points. The concentration of ^{13}C-pyruvate in highly perfused organs may be supraphysiologic and may therefore saturate the enzymatic reactions, whereas in slower perfused tumors the effectively arriving dose may actually be suboptimally low. Often bidirectional exchange may occur between the identified metabolite compartments, and competitive substrate pathways may dilute the ^{13}C-signal. Therefore, the quantitative measurement of unidirectional fluxes may be limited by the currently used ^{13}C-MRSI technique. This increased sensitivity to metabolic dynamics and the short acquisition time, however, at the same time require more careful control of [1-^{13}C]pyruvate application and metabolic conditions than initially anticipated. These observations, in fact, constitute the main finding of the study, suggesting the feasibility of identifying tumor tissue with increased lactate production. Complementary information is provided by ^{18}F-FDG and ^{13}C metabolite measurements in HCC tumor–bearing rats, possibly helping in the future with dissection of metabolic pathways in vivo.

The evaluation of reproducibility and robustness of metabolic ^{13}C MRSI measurements in tumor tissue while optimizing ^{13}C MRSI data acquisition schemes will be the focus of our future work.

CONCLUSION

The presented work demonstrated that dynamic CSI using ^{13}C pyruvate allows for the in vivo assessment of regional metabolism in tumor tissue. Transplanted tumor cells exhibited increased glycolytic flux as demonstrated by increased ^{18}F-FDG uptake and locally increased conversion of pyruvate to lactate. In the model of xenotransplanted tumors with nonphysiologic perfusion, lactate signal in tumor tissue exhibited high variability most likely reflecting signal loss due to slow delivery and rapid depolarization in the cases of low TMR. Further methodologic improvements may be needed to increase the sensitivity of this new imaging approach. The quantitative information provided by ^{13}C MRSI may be useful in assessing tumor metabolism after therapeutic intervention, as already shown by nonimaging studies with ^{13}C pyruvate (*11*). The combination of ^{18}F-FDG PET and ^{13}C MRSI may be attractive for future research studies to probe metabolic pathways with high sensitivity and specificity and for cross-validation of new metabolic imaging protocols.

DISCLOSURE

The costs of publication of this article were defrayed in part by the payment of page charges. Therefore, and solely to indicate this fact, this article is hereby marked "advertisement" in accordance with 18 USC section 1734. This work was supported by a grant from the German Bundesministerium für Bildung und Forschung (BMBF MOBITUM grant no. FKZ 01EZ0826/7). The authors take responsibility for the content of the publication. No other potential conflict of interest relevant to this article was reported.

ACKNOWLEDGMENTS

We thank Guido Kudielka for MR system support; Steffen Grott for support with ^{13}C metabolic data processing; Sandra van Marwick for support with the Munich Heart M3P Anima software; and Jan Henrik Ardenkjær-Larsen, Per Åkesson, Ralph E. Hurd, and Albert P. Chen for helpful discussion.

REFERENCES

1. Warburg O, Wind F, Negelein E. The metabolism of tumors in the body. *J Gen Physiol.* 1927;8:519–530.
2. Phelps ME, Huang SC, Hoffman EJ, Selin C, Sokoloff L, Kuhl DE. Tomographic measurement of local cerebral glucose metabolic rate in humans with (F-18)2-fluoro-2-deoxy-D-glucose: validation of method. *Ann Neurol.* 1979;6:371–388.

Downloaded from jnm.snmjournals.org by on March 14, 2017. For personal use only.

3. Carruthers A. Facilitated diffusion of glucose. *Physiol Rev.* 1990;70:1135–1176.
4. Gatley SJ. Iodine-123-labeled glucose analogs: prospects for a single-photon-emitting analog of fluorine-18-labeled deoxyglucose. *Nucl Med Biol.* 1995;22: 829–835.
5. Blodgett TM, Meltzer CC, Townsend DW. PET/CT: form and function. *Radiology.* 2007;242:360–385.
6. Rohren EM, Turkington TG, Coleman RE. Clinical applications of PET in oncology. *Radiology.* 2004;231:305–332.
7. Abouzied MM, Crawford ES, Nabi HA. ^{18}F-FDG imaging: pitfalls and artifacts. *J Nucl Med Technol.* 2005;33:145–155.
8. Haberkorn U, Markert A, Mier W, Askoxylakis V, Altmann A. Molecular imaging of tumor metabolism and apoptosis. *Oncogene.* 2011;30:4141–4151.
9. Kurhanewicz J, Vigneron DB, Brindle K. Analysis of cancer metabolism by imaging hyperpolarized nuclei: prospects for translation to clinical research. *Neoplasia.* 2011;13:81–97.
10. Gallagher FA, Bohndiek SE, Kettunen MI, Lewis DY, Soloviev D, Brindle KM. Hyperpolarized ^{13}C MR imaging and PET: in vivo tumor biochemistry. *J Nucl Med.* 2011;52:1333–1336.
11. Day SE, Kettunen MI, Gallagher FA, et al. Detecting tumor response to treatment using hyperpolarized ^{13}C magnetic resonance imaging and spectroscopy. *Nat Med.* 2007;13:1382–1387.
12. Brindle KM. NMR methods for measuring enzyme kinetics in vivo. *Prog Nucl Magn Reson Spectrosc.* 1988;20:257–293.
13. Ardenkjaer-Larsen JH, Fridlund B, Gram A, et al. Increase in signal-to-noise ratio of > 10,000 times in liquid-state NMR. *Proc Natl Acad Sci USA.* 2003;100: 10158–10163.
14. Golman K, Ardenkjaer-Larsen JH, Petersson JS, Månsson S, Leuenbach I. Molecular imaging with endogenous substances. *Proc Natl Acad Sci USA.* 2003;100:10435–10439.
15. Witney TH, Kettunen MI, Brindle KM. Kinetic modeling of hyperpolarized ^{13}C label exchange between pyruvate and lactate in tumor cells. *J Biol Chem.* 2011; 286:24572–24580.
16. Feron O. Pyruvate into lactate and back: from the Warburg effect to symbiotic energy fuel exchange in cancer cells. *Radiother Oncol.* 2009;92:329–333.
17. Boctor ZN, El-Hilali MM. Lactate dehydrogenase isoenzymes in carcinoma of the bladder: a clinical study. *J Surg Oncol.* 1969;1:199–203.
18. Walenta S, Wetterling M, Lehrke M, et al. High lactate levels predict likelihood of metastases, tumor recurrence, and restricted patient survival in human cervical cancers. *Cancer Res.* 2000;60:916–921.
19. Albers MJ, Bok R, Chen AP, et al. Hyperpolarized ^{13}C lactate, pyruvate, and alanine: noninvasive biomarkers for prostate cancer detection and grading. *Cancer Res.* 2008;68:8607–8615.
20. Mayer D, Yen YF, Takahashi A, et al. Dynamic and high-resolution metabolic imaging of hyperpolarized [1-^{13}C]-pyruvate in the rat brain using a high-performance gradient insert. *Magn Reson Med.* 2011;65:1228–1233.
21. Wiesinger F, Weidl E, Menzel MI, et al. IDEAL spiral CSI for dynamic metabolic MR imaging of hyperpolarized [1-^{13}C]pyruvate. *Magn Reson Med.* 2012;68:8–16.
22. Schulte RF, Sperl JI, Weidl E, et al. Saturation-recovery metabolic-exchange rate imaging with hyperpolarized [1-^{13}C] pyruvate using spectral-spatial excitation. *Magn Reson Med.* May 30, 2012 [Epub ahead of print].
23. Josan S, Spielman D, Yen YF, Hurd R, Pfefferbaum A, Mayer D. Fast volumetric imaging of ethanol metabolism in rat liver with hyperpolarized [1-^{13}C]pyruvate. *NMR Biomed.* 2012;25:993–999.
24. Janich MA, Menzel MI, Wiesinger F, et al. Effects of pyruvate dose on in vivo metabolism and quantification of hyperpolarized ^{13}C spectra. *NMR Biomed.* 2012;25:142–151.
25. Atherton HJ, Schroeder MA, Dodd MS, et al. Validation of the in vivo assessment of pyruvate dehydrogenase activity using hyperpolarised ^{13}C MRS. *NMR Biomed.* 2011;24:201–208.
26. Fahey FH, Gage HD, Buchheimer N, et al. Evaluation of the quantitative capability of a high-resolution positron emission tomography scanner for small animal imaging. *J Comput Assist Tomogr.* 2004;28:842–848.
27. Derby KT, Hawryszko C. Design and evaluation of a novel dual-tuned 6 resonator for spectroscopic imaging. *J Magn Reson.* 1990;86:645–651.
28. Patlak CS, Blasberg RG. Graphical evaluation of blood-to-brain transfer constants from multiple-time uptake data: generalizations. *J Cereb Blood Flow Metab.* 1985;5:584–590.
29. Otto AM, Muller CS, Huff T, Hannappel E. Chemotherapeutic drugs change actin skeleton organization and the expression of beta-thymosins in human breast cancer cells. *J Cancer Res Clin Oncol.* 2002;128:247–256.
30. Larson PE, Bok R, Kerr AB, et al. Investigation of tumor hyperpolarized [1-^{13}C]-pyruvate dynamics using time-resolved multiband RF excitation echo-planar MRSI. *Magn Reson Med.* 2010;63:582–591.
31. Darpolor MM, Yen YF, Chua MS, et al. In vivo MRSI of hyperpolarized [1-^{13}C] pyruvate metabolism in rat hepatocellular carcinoma. *NMR Biomed.* 2011;24:506–513.
32. Bagi CM, Andresen CJ. Models of hepatocellular carcinoma and biomarker strategy. *Cancers.* 2010;2:1441–1452.
33. Killion JJ, Radinsky R, Fidler IJ. Orthotopic models are necessary to predict therapy of transplantable tumors in mice. *Cancer Metastasis Rev.* 1998–1999;17:279–284.
34. Lau AZ, Chen AP, Ghugre NR, et al. Rapid multislice imaging of hyperpolarized ^{13}C pyruvate and bicarbonate in the heart. *Magn Reson Med.* 2010;64:1323–1331.
35. Lau AZ, Chen AP, Hurd RE, Cunningham CH. Spectral-spatial excitation for rapid imaging of DNP compounds. *NMR Biomed.* 2011;24:988–996.

Downloaded from jnm.snmjournals.org by on March 14, 2017. For personal use only.

The Journal of NUCLEAR MEDICINE

Multimodal Assessment of In Vivo Metabolism with Hyperpolarized [1-^{13}C]MR Spectroscopy and ^{18}F-FDG PET Imaging in Hepatocellular Carcinoma Tumor–Bearing Rats

Marion I. Menzel, Eliane V. Farrell, Martin A. Janich, Oleksandr Khegai, Florian Wiesinger, Stephan Nekolla, Angela M. Otto, Axel Haase, Rolf F. Schulte and Markus Schwaiger

J Nucl Med. 2013;54:1113-1119.
Published online: April 17, 2013.
Doi: 10.2967/jnumed.112.110825

This article and updated information are available at:
http://jnm.snmjournals.org/content/54/7/1113

Information about reproducing figures, tables, or other portions of this article can be found online at:
http://jnm.snmjournals.org/site/misc/permission.xhtml

Information about subscriptions to JNM can be found at:
http://jnm.snmjournals.org/site/subscriptions/online.xhtml

The Journal of Nuclear Medicine is published monthly.
SNMMI | Society of Nuclear Medicine and Molecular Imaging
1850 Samuel Morse Drive, Reston, VA 20190.
(Print ISSN: 0161-5505, Online ISSN: 2159-662X)

© Copyright 2013 SNMMI; all rights reserved.

SNMMI SOCIETY OF NUCLEAR MEDICINE AND MOLECULAR IMAGING